

Article

New Insights into the Magnetic Properties of CoFe₂O₄@SiO₂@Au Magnetoplasmonic Nanoparticles

Rareș Bortnic¹, Adam Szatmari¹, Gabriela Souca¹, Răzvan Hirian¹, Roxana Dudric¹, Lucian Barbu-Tudoran^{2,3}, Valentin Toma⁴ , Rareș Știufiuc⁴ , Romulus Tetean^{1,*} and Emil Burzo¹

¹ Faculty of Physics, “Babes Bolyai” University, 400084 Cluj-Napoca, Romania; rares.bortnic@ubbcluj.ro (R.B.); adam.szatmari@ubbcluj.ro (A.S.); gabriela.souca@ubbcluj.ro (G.S.); razvan.hirian@ubbcluj.ro (R.H.); roxana.dudric@ubbcluj.ro (R.D.); emil.burzo@ubbcluj.ro (E.B.)

² Electron Microscopy Center “Prof. C. Crăciun”, Faculty of Biology & Geology, “Babes-Bolyai” University, 400006 Cluj-Napoca, Romania; lucian.barbu@itim-cj.ro

³ Integrated Electron Microscopy Laboratory, National Institute for Research and Development of Isotopic and Molecular Technologies, 400293 Cluj-Napoca, Romania

⁴ Department of Bionanoscopia, MedFuture Research Center for Advance Medicine, “Tuliu Hatieganu” University of Medicine and Pharmacy, 400337 Cluj-Napoca, Romania; valentin.toma@umfcluj.ro (V.T.); rares.stiufiuc@umfcluj.ro (R.Ș.)

* Correspondence: romulus.tetean@ubbcluj.ro; Tel.: +40-741033325

Abstract: We report the successful synthesis and a complete magnetic characterization of CoFe₂O₄@SiO₂@Au magnetoplasmonic nanoparticles. The CoFe₂O₄ magnetic nanoparticles were prepared using the hydrothermal method. A subsequent SiO₂ shell followed by a plasmonic Au shell were deposited on the magnetic core creating magnetoplasmonic nanoparticles with a core–shell architecture. A spin-glass-type magnetism was shown at the surface of the CoFe₂O₄ nanograins. Depending on the external magnetic field, two types of spin-glass were identified and analyzed in correlation with the exchange field acting on octahedral and tetrahedral iron sites. The magnetization per formula unit of the CoFe₂O₄ core is not changed in the case of CoFe₂O₄@SiO₂@Au nanocomposites. The gold nanoparticles creating the plasmonic shell show a giant diamagnetic susceptibility, dependent on their crystallite sizes.

Keywords: core–shell nanoparticles; magnetoplasmonic nanoparticles; magnetic properties; spin-glass; exchange field



Citation: Bortnic, R.; Szatmari, A.; Souca, G.; Hirian, R.; Dudric, R.; Barbu-Tudoran, L.; Toma, V.; Știufiuc, R.; Tetean, R.; Burzo, E. New Insights into the Magnetic Properties of CoFe₂O₄@SiO₂@Au Magnetoplasmonic Nanoparticles. *Nanomaterials* **2022**, *12*, 942. <https://doi.org/10.3390/nano12060942>

Academic Editor:
Alessandro Lascialfari

Received: 20 February 2022

Accepted: 10 March 2022

Published: 12 March 2022

Publisher’s Note: MDPI stays neutral with regard to jurisdictional claims in published maps and institutional affiliations.



Copyright: © 2022 by the authors. Licensee MDPI, Basel, Switzerland. This article is an open access article distributed under the terms and conditions of the Creative Commons Attribution (CC BY) license (<https://creativecommons.org/licenses/by/4.0/>).

1. Introduction

The flexibility of spinel ferrite CoFe₂O₄ or a (Co_{1-x}Fe_x)_T(Co_xFe_{2-x})_OO₄ structure, with a variable occupancy of tetrahedral (T) and octahedral sites (O), provides a wide range of physical properties and applications, particularly in their nanosized form. As a function of the inversion parameter, x , the structure changes from a normal spinel ($x = 0$) to an inverse spinel type ($x = 1$). In a bulk state, the CoFe₂O₄ ferrite has mainly an inverse-type spinel structure and crystallizes in an FCC-type lattice, space group $Fm\bar{3}m$. The ferrite is ferrimagnetically ordered, and the magnetic moments of the atoms situated in octahedral and tetrahedral sublattices, respectively, being antiparallely aligned. According to the degree of inversion, a large range of magnetizations can be obtained. The superexchange parameters inside and between magnetic sublattices were determined in the bulk state, starting from a mean field model [1,2].

At the nanometer scale, the magnetic behavior of CoFe₂O₄ ferrite shows significant differences with respect to that of the bulk state. The crossover to a single domain behavior is 40 nm [3]. The system becomes superparamagnetic between 7 and 10 nm. A core–shell model was proposed for CoFe₂O₄ nanograins, in which a core of aligned spins is surrounded by a magnetically disordered shell [4]. The low-temperature magnetic behavior of ultra-small CoFe₂O₄ nanoparticles was also associated with a random freezing of surface

spins [5,6]. Thus, associated with size reduction and the formation of single-domain particles, the presence of superparamagnetism, a canted spin structure and surface anisotropy can be present, with different potential applications such as biomedical, electrical, antibacterial, energy storage media, coatings and magnetic refrigerants [7–10].

The CoFe_2O_4 nanoparticles are difficult to disperse due to their strong magnetic properties. A method to suppress nanoparticles' agglomeration consists in surface modification by coating, leading to the creation of so-called core-shell nanocomposites. For medical applications, the coating shell must be non-toxic, biocompatible and stable in physiological environments. A silica shell protects and stabilizes the magnetic core, in addition to having low cytotoxicity, good chemical inertness and high thermal stability [9–12]. Additionally, it can be functionalized to bind on its surface molecules that possess silanol groups.

The magnetoplasmonic core-shell nanocomposites, having a noble metal shell, are promising materials for biomedical applications. Metallic Au and Ag have a good surface-enhanced Raman scattering effect, whose surface plasma resonance enhances the electromagnetic field near the surface [13–17]. In this way the Raman scattering signals of the adsorbed molecules are greatly enhanced as compared with that of the ordinary Raman molecules. The gold does not interact with biological systems, so the use of Au on the shell surface is useful in supplying biocompatibility characteristics to nanostructures.

The present paper reports the successful synthesis and physical characterization of $\text{CoFe}_2\text{O}_4@SiO_2@Au$ magnetoplasmonic nanoparticles. The CoFe_2O_4 magnetic nanoparticles have been synthesized by the hydrothermal method. Subsequently, the SiO_2 shell was deposited on CoFe_2O_4 core nanoparticles. The further deposition of gold was made after the functionalization of $\text{CoFe}_2\text{O}_4@SiO_2$ nanocomposites. Once the synthesis process was completed, a complete evaluation of their magnetic properties has been performed. A spin-glass-type magnetism was identified at the surface of CoFe_2O_4 nanograins. The magnetization per formula unit of CoFe_2O_4 core was not changed in the $\text{CoFe}_2\text{O}_4@SiO_2@Au$ nanocomposites, while the coercive fields decreased in the case of magneto-plasmonic nanohybrids. The gold nanoparticles on the shell showed a giant diamagnetic susceptibility, dependent on their crystallite sizes.

2. Materials and Methods

2.1. Samples Preparation

The CoFe_2O_4 nanoparticles were prepared using a typical hydrothermal method [18,19]. The Fe(III)acetylacetonate (0.4 mmol) and Co(II) acetylacetonate (0.2 mmol) were dissolved in 55 mL ethylene glycol and kept at a temperature of 50 °C. Following this, 0.8 g of polyvinylpyrrolidone (PVP) was added to the solution. After magnetic stirring, the above solution was transferred to an autoclave, and heated to 240 °C at a rate of 0.3 °C/min and maintained at this temperature for 12 h. After cooling, the resulting product was washed several times using a 4/1 volumetric ratio of diethyl ether and ethanol. The CoFe_2O_4 nanoparticles were obtained by drying the solution at 50 °C.

In order to deposit the SiO_2 shell on CoFe_2O_4 nanoparticles, the Stober method was employed. The CoFe_2O_4 nanoparticles (0.2 mmol) were dispersed in 80 mL ethanol by ultrasonication and mechanical stirring; the dispersed particles were functionalized using 0.2 mL APTES. After ultrasonication and mechanical stirring, the shell deposition was completed during further sonication by adding TEOS (0.2 mL) to the solution and by increasing the pH upon the addition of the NH_4OH solution. The solution was sonicated and stirred for 2 h, keeping the temperature constant at $t = 40$ °C. The nanocomposites thus obtained were washed several times with ethanol and then dispersed in water.

The $\text{CoFe}_2\text{O}_4@SiO_2$ nanostructures were then functionalized with 0.2 mL of 3-aminopropyltriethoxysilane (APTES.) The obtained $\text{CoFe}_2\text{O}_4@SiO_2$ particles were dispersed in water. The pH of the solution was lowered to 4 using a 1M HCl solution. Aqueous solutions of chloroauric acid (20 mmol/L), sodium citrate dehydrate (100 mmol/L), mixed trisodium citrate dehydrate (20 mmol/L) and sodium borohydride (50 mmol/L) were added sequentially and dropwise during sonification and mechanical stirring. The tem-

perature was kept at 65 °C. Three series were prepared, denoted $\text{CoFe}_2\text{O}_4@\text{SiO}_2@\text{AuN}$ ($N = 1-3$). Finally, the nanocomposites were then washed.

2.2. Characterization

The morphology of the CoFe_2O_4 nanoparticles and of the $\text{CoFe}_2\text{O}_4@\text{SiO}_2@\text{AuN}$ nanocomposites was investigated by transmission electron microscopy (TEM) and scanning electron microscopy (SEM) using a Hitachi HD2700. The EDS measurements were done in order to analyze the composition of the prepared nanocomposites.

The crystal structure and crystallite sizes of CoFe_2O_4 nanoparticles and of the $\text{CoFe}_2\text{O}_4@\text{SiO}_2@\text{AuN}$ nanocomposites were determined by XRD measurements, performed at ambient temperature, with a Bruker D8 Advance diffractometer. The crystallite sizes were estimated by Rietveld refinement of XRD patterns, using FullProf Suite software.

Magnetic measurements were performed in the 4.2–300 K temperature range, and in external magnetic fields of up to 12 T, using a vibrating sample magnetometer from Cryogenic Limited (London, UK).

3. Results

3.1. Morphology and Crystal Structure

The XRD patterns of CoFe_2O_4 and $\text{CoFe}_2\text{O}_4@\text{SiO}_2@\text{AuN}$ nanocomposites are shown in Figure 1. As expected, they correspond to the superposition of the XRD lines of CoFe_2O_4 and Au (ICDD PDF: 22-1086 for CoFe_2O_4 and 98-005-0876 for Au). All diffraction peaks including (111), (220), (311), (400), (422), (511) and (440) are fully indexed to the spinel CoFe_2O_4 phase. The sharp peaks corresponding to the (111), (200), (220) and (311) planes shown in the $\text{CoFe}_2\text{O}_4@\text{SiO}_2@\text{AuN}$ nanocomposite patterns confirm the crystallization of cubic FCC Au. The SiO_2 was in amorphous state, as evidenced in XRD patterns by a broad feature at low angles. The lattice constants of CoFe_2O_4 and Au, determined from Rietveld refinements, are not dependent on nanostructures compositions and close to those of bulk samples. The crystallite sizes of CoFe_2O_4 nanoparticles are in the 14.2 nm and 20.2 nm range, while those of the gold nanoparticles were found to be between 15.9 nm and 23.6 nm (Table 1).

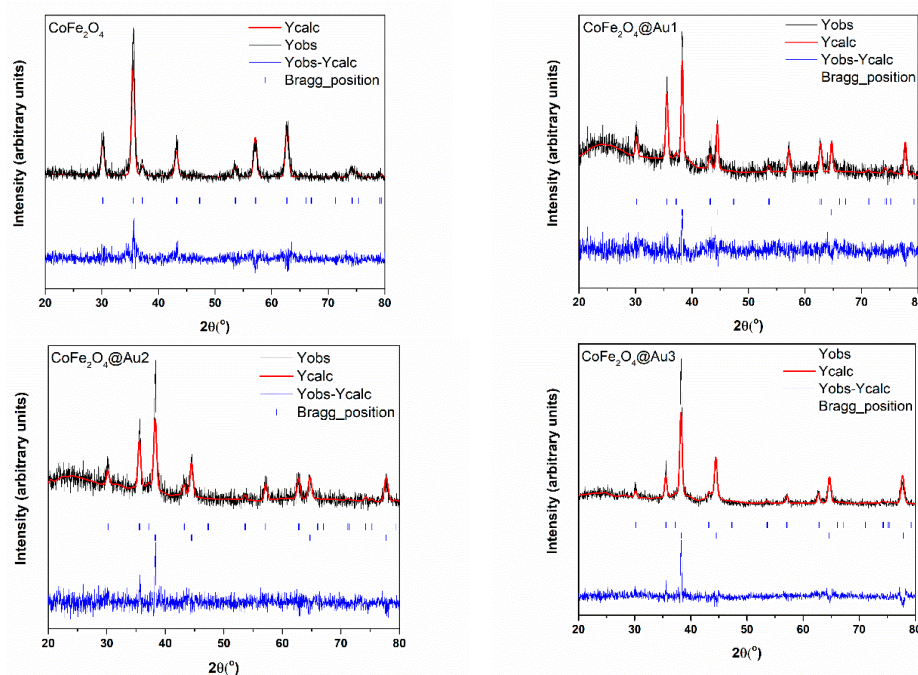


Figure 1. XRD patterns of CoFe_2O_4 and $\text{CoFe}_2\text{O}_4@\text{SiO}_2@\text{Au}$ nanocomposites and the results of Rietveld refinements.

Table 1. Compositions, lattice parameters, crystallites sizes, magnetizations and coercive fields. AuN is a symbol for $\text{CoFe}_2\text{O}_4@\text{SiO}_2@\text{AuN}$ nanostructures with $N = 1-3$).

| Nanostructure | | CoFe_2O_4 | Au1 | Au2 | Au3 |
|-------------------------------------------------------------------------------|--------------------------------|---------------------------|------------|------------|------------|
| Composition (weight %) | CoFe_2O_4 | 100 | 46.8 | 41.8 | 24.3 |
| | SiO_2 | - | 11.0 | 11.6 | 6.3 |
| | Au | - | 42.2 | 46.6 | 69.4 |
| Lattice parameter (nm) | CoFe_2O_4 core | 0.8379 (9) | 0.8375 (4) | 0.8372 (9) | 0.8376 (9) |
| Crystallite size (nm) | | 14.2 (2) | 20.2 (3) | 17.3 (2) | 20.2 (2) |
| Lattice parameter (nm) | Au shell | - | 0.4073 (2) | 0.4073 (9) | 0.4074 (7) |
| Crystallite size (nm) | | - | 23.57 (2) | 15.86 (4) | 18.88 (6) |
| Nanocomposite magnetization/ CoFe_2O_4 weight percent (emu/g) | | 86.9 | 86.1 | 84.5 | 85.5 |
| Coercive field H_C (T) | $T = 4.2$ k | 0.35 | 0.20 | 0.28 | 0.19 |
| | $T = 300$ k | 0.04 | 0.03 | 0.03 | 0.030 |

The TEM and SEM images of CoFe_2O_4 nanoparticles evidenced that these were of nearly spherical form and agglomerated in separate pseudo-spherical “raspberry”-like nanostructures, with an average particle size of approximately 79 nm (Figure 2a,b). The mean size of the crystallites was around 19 nm, as can be seen in Figure 2c.

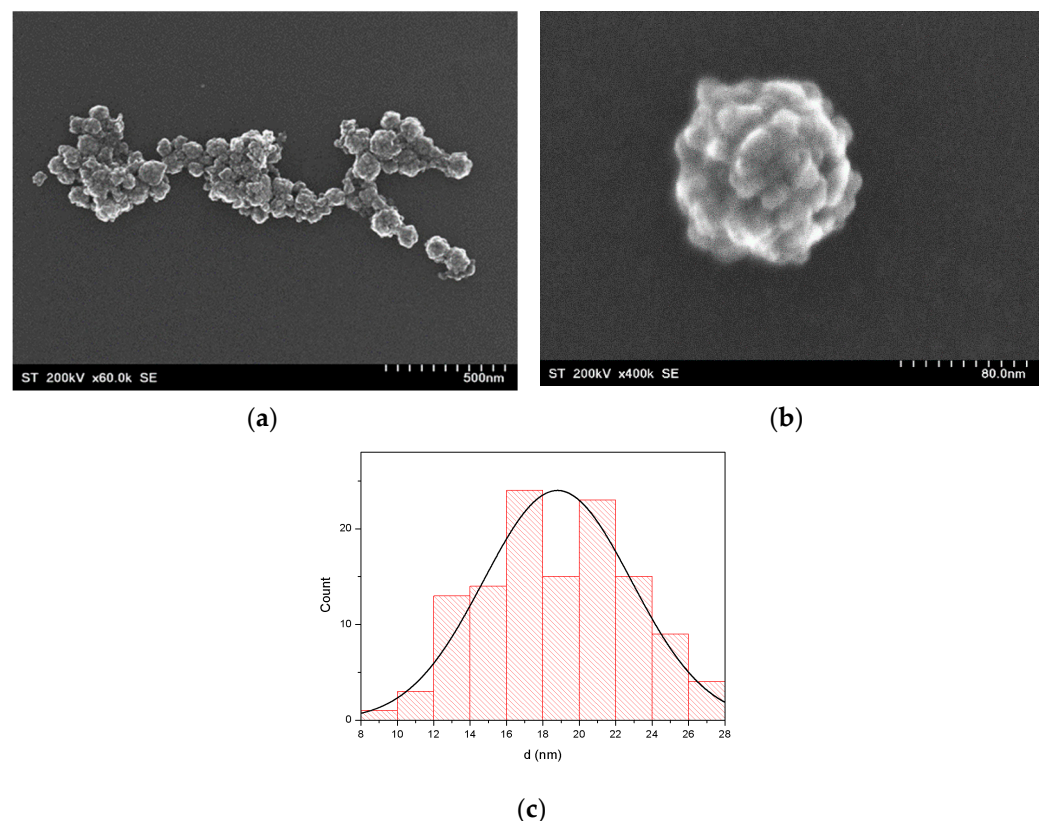


Figure 2. SEM images of CoFe_2O_4 nanoparticles (a,b) and particle size histogram (c).

After the deposition of SiO_2 , the TEM images show the formation of a shell layer (Figure 3). The nanocomposites thus formed had spherical or pseudo-spherical forms. A similar morphology was shown after gold deposition (Figure 4). The core-shell $\text{CoFe}_2\text{O}_4@\text{SiO}_2@\text{AuN}$ nanoparticles were nearly completely covered by gold. High resolution pictures confirmed that the Au nanoparticles had dimensions close to those determined

by SEM, being in the 14–21 nm range. The average size of these nanocomposites was 288(57) nm.

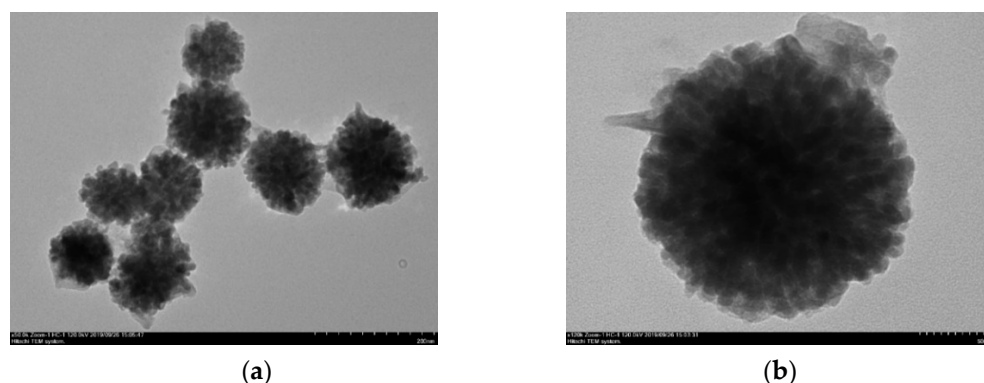


Figure 3. TEM images of $\text{CoFe}_2\text{O}_4@SiO_2$ nanostructures (a) and of one isolated nanoparticle (b).

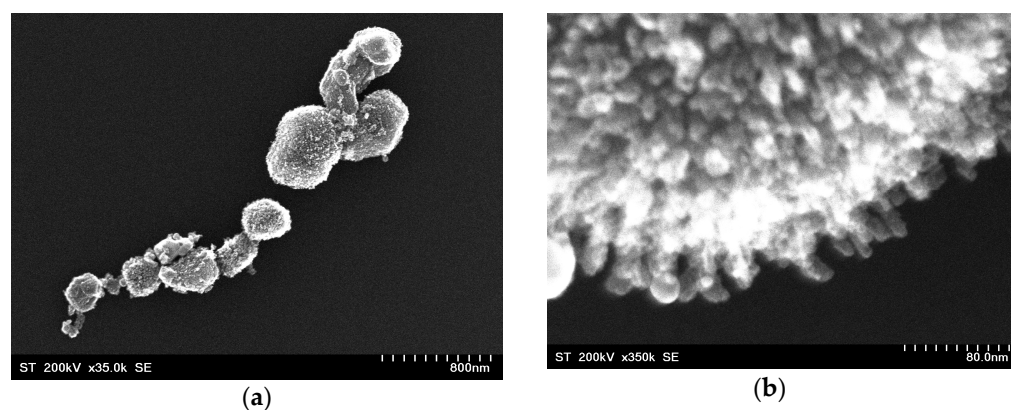


Figure 4. SEM images of $\text{CoFe}_2\text{O}_4@SiO_2@Au_2$ nanocomposite (a) and the edge of a nanoparticle.

The EDS results show that the nanocomposites consisted of Fe, Co, O, Si and Au. As an example, the EDS results for $\text{CoFe}_2\text{O}_4@SiO_2@Au_2$ are given in Figure 5. The compositions determined for the studied samples are listed in Table 1.

3.2. Magnetic Properties

The magnetization isotherms, recorded at $T = 4.2$ K and 300 K for nanocrystalline CoFe_2O_4 and $\text{CoFe}_2\text{O}_4@SiO_2@AuN$ nanostructures, are shown in Figure 6. The presence of a spin-glass contribution superposed on mainly ferrimagnetic-type ordering is suggested in CoFe_2O_4 nanocrystalline samples by the present investigations. The spin canting could have been present due to the following: (1) surface effects due to symmetry breaking by the broken exchange bonds at the surface layer, (2) cation distribution in the tetrahedral and octahedral sites and (3) interactions between nanoparticles. In a spin-glass system, instead of having global anisotropy axes, there are easy axes whose directions vary randomly in space. Their direction is determined by the local spin arrangement.

The previous Mössbauer studies [5,6] as well as infrared spectroscopy [4] performed on CoFe_2O_4 nanocrystalline samples evidenced the presence of a spin-glass state. It can be mentioned that in a large number of studies, ferrimagnetic-type behavior was also reported. The field dependences of the magnetization, in a spin-glass system, have been already analyzed [20]. In such a system, which shows high anisotropy (correlated spin glass), the approach to magnetic saturation follows a $1/H^2$ law. In systems with weak anisotropy (a ferromagnet with wandering axes) the approach to saturation when the external field, H , is smaller than the exchange field, H_{ex} , can be described by a $1/H^{1/2}$ dependence, while for $H > H_{ex}$ it follows the same dependence as for systems having high anisotropy. The

spin-glass state of surface magnetization of weak anisotropic perovskites is well described by the $1/H^{1/2}$ law, as already reported [21–23].

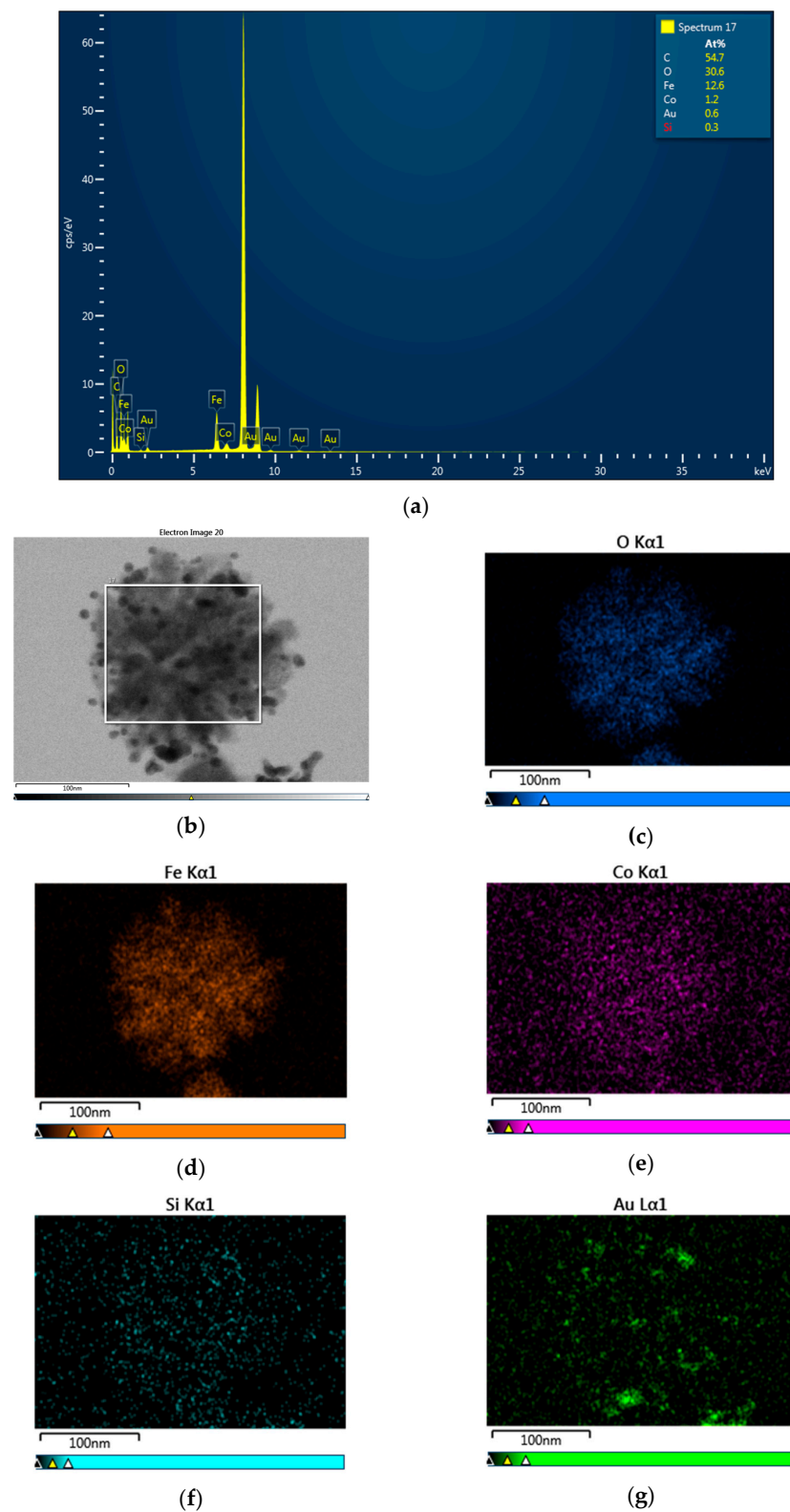


Figure 5. EDS spectrum (a), TEM image (b) EDS mapping (c–g) of $\text{CoFe}_2\text{O}_4@SiO_2@Au_2$ nanocomposite.

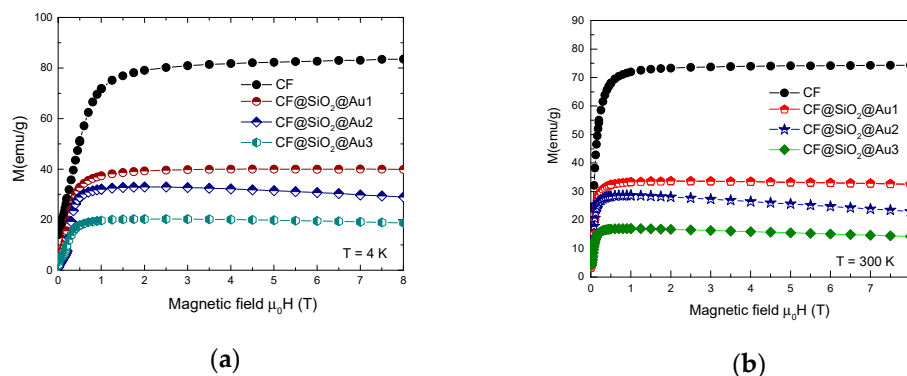


Figure 6. Magnetization isotherms at $T = 4.2$ K (a) and $T = 300$ K (b) of CoFe_2O_4 and $\text{CoFe}_2\text{O}_4@SiO_2@Au$ nanocomposites.

The analysis of magnetization isotherms in CoFe_2O_4 nanograins suggests the presence of a spin-glass state superposed on mainly ferrimagnetic-type behavior. The dependences of magnetizations, at $T = 4.2$ K and 300 K on $1/H^{1/2}$, are given in Figure 7. Linear variations are present in the field ranges up to 12 T, for data obtained at $T = 300$ K and up to $\mu_0H = 8$ T at $T = 4.2$ K, described by the relation:

$$\frac{M(H)}{M(0)} = 1 - bH^{-1/2} \tag{1}$$

with a rate $b = 0.1275$ ($T^{1/2}$) at $T = 4.2$ K and 0.0402 ($T^{1/2}$) at $T = 300$ K. Nearly the same rate b has been obtained at $T = 4.2$ K for the field dependence of magnetization at the grain surface of $\text{Sr}_2\text{FeMoO}_6$ -based perovskites [22,23].

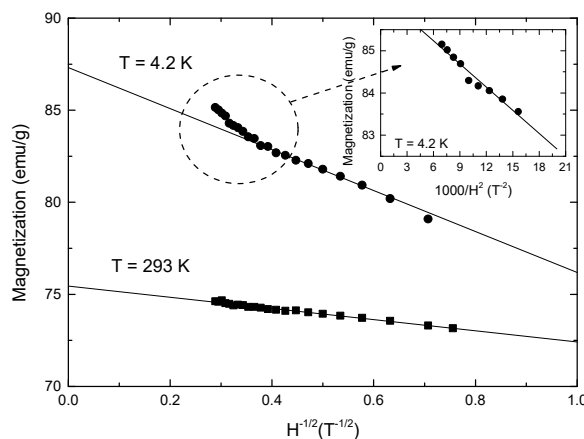


Figure 7. Magnetization isotherms of CoFe_2O_4 at $T = 4.2$ K and $T = 300$ K as function of $H^{1/2}$. In inset, the data at $T = 4.2$ K for $H > 8$ T as a function of H^{-2} .

For fields higher than 8–9 T, the magnetization at 4.2 K follows a $1/H^2$ law. There is a change in the shell magnetic behavior, suggesting a transition from a spin-glass state with wandering axes to a correlated spin-glass state. The extrapolation of magnetizations at $T = 4.2$ K, for both $1/H^{1/2}$ and $1/H^2$ trends, to infinite field, as expected, give the same value of saturation magnetization, $M_s = 87.0$ (3) emu/g. This corresponds to a magnetic moment per formula unit of $M_s = 3.65 \mu_B/\text{fu}$ and it is expected to characterize the situation when the moments of both core and shell are oriented along the same axis. Thus, the inversion factor can be determined from saturation magnetization [24,25] as being $x = (1/4)(7 - M_s) = 0.838$. The composition of the sample $(\text{Co}_{0.162}\text{Fe}_{0.838})_T(\text{Co}_{0.838}\text{Fe}_{1.162})_O\text{O}_4$ is closer to that of an inverse-spinel-type structure.

The analysis of magnetization at $T = 4.2$ K suggests that the contribution of the spin-glass state to magnetization is around 8% of the total nanoparticle magnetization. This could be due to the cumulative effects of the broken exchange bonds at the surface layer, as well as to the exchange interactions between constituent ions, assuming a spherical grain with $d = 20$ nm and the shell volume having one CoFe_2O_4 lattice parameter (0.4 nm) width, corresponding to 11% of that of the nanograin. By Mössbauer spectroscopy, it was shown that the canting angle of iron moments in CoFe_2O_4 at tetrahedral sites was 41° and at octahedral sites 36° [5]. Thus, the corresponding magnetization of the shell volume, on the field direction, was $\sim 8\%$ of the total magnetization, suggesting that the spin-glass state is mainly due to the surface shell.

The exchange interactions at the level of the unit cell also influences the spin canting. The anisotropy of cobalt is sensitively higher than that of iron and no canting is expected for cobalt moments, unlike for the Fe^{3+} spins. The exchange fields acting on iron ions in octahedral and tetrahedral sites were estimated starting from the exchange interaction parameters in bulk CoFe_2O_4 , determined in the mean field model, assuming the presence of two [1] or three [2] magnetic sublattices. According to the determined inversion parameter, a tetrahedral Fe^{3+} ion has as neighbors four Fe and two Co octahedral ions, and an octahedral Fe^{3+} ion seven Co and five Fe tetrahedral ions, respectively [6]. In the above assumptions, the exchange fields, H_{ex} , acting on iron at octahedral and tetrahedral sites are roughly of 300 T and 160 T, respectively. These values approximate those of the nanoparticle core. The exchange fields at the surface layer are sensitively diminished due to broken bonds and deviations from the parallel alignment of iron moments. Thus, for tetrahedral iron sites, in the one lattice parameter shell, the exchange field can be of a magnitude not highly different from the external field used for measurements. Consequently, there can be different magnetic responses of Fe^{3+} ions at tetrahedral and octahedral sites in the presence of an external field.

At ambient temperature, only a $T^{-1/2}$ dependence of surface magnetization is shown, as determined by thermal effects.

The nanoparticle anisotropy seems to influence also the spin-canting-type behavior. The hysteresis curves recorded at 4.2 K and 300 K are given in Figure 8. At $T = 4.2$ K, the remanent magnetization was $M_r/M_s = 0.5$, as expected for single domain particles. A smaller M_r/M_s value was obtained at $T = 300$ K, correlated with the superparamagnetism of some nanoparticles having dimensions $d < 10$ nm—see Figure 8b. The anisotropy constants of CoFe_2O_4 nanoparticles were estimated assuming that below the blocking temperature, T_B the anisotropy is uniaxial [26]. According to the Stoner–Wohlfarth model for non-interacting single domain particles, the coercive field, H_c , depends both on the anisotropy constant K_1 and saturation magnetization [27]:

$$H_c = 2K_1 / \mu_0 M_s \quad (2)$$

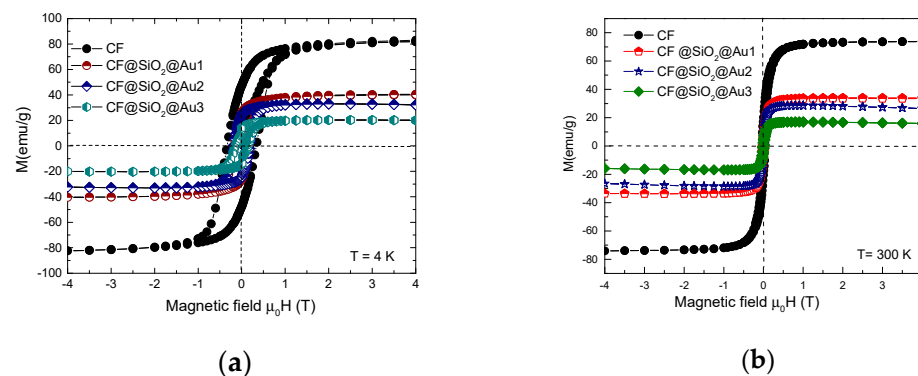


Figure 8. Hysteresis loops of $\text{CoFe}_2\text{O}_4@SiO_2@Au$ nanoparticles at $T = 4.2$ K (a) and $T = 300$ K (b).

From experimentally determined H_c values, anisotropy constants $K_1 = 7 \times 10^5$ ($T = 4.2$ K) and 6.8×10^4 ($T = 300$ K) J/m^3 were obtained.

The effective anisotropy constant, K_{eff} , has been estimated using the blocking temperature T_B , according to the relation:

$$T_B = K_{\text{eff}}V/25k_B \quad (3)$$

where V is the nanoparticle volume.

For a log normal distribution of particles sizes, the blocking temperature, T_B , is related to the temperature corresponding to the maximum in ZFC magnetization, T_{max} , by the relation [28]: $T_{\text{max}} = e\langle T_B \rangle$, where e is in the 1.5–2.5 range. A careful analysis of the matter in case of CoFe_2O_4 nanoparticles with dimensions 5–7 nm evidenced a value $e = 1.70$ [29]. By using this value and taking into account that $T_{\text{max}} = 300$ K, an effective anisotropy constant $K_{\text{eff}} = 4.31 \times 10^4$ J/m^3 was estimated assuming crystallite sizes of 15 nm. This value is close to that determined at $T = 300$ K from a coercive field. Somewhat higher K_{eff} values were obtained for nanograins with dimensions of 6.6 nm [16]. Starting from the determined anisotropy constants, the anisotropy field $H_a = 2K/\mu_0M$ of 9–14 T was estimated. These values are smaller than the exchange field, but close to the field where a change in the spin-glass-type behavior was shown, suggesting possible relations.

The magnetization isotherms for $\text{CoFe}_2\text{O}_4@SiO_2@AuN$ nanostructures can be described by the contributions of a magnetic ordered phase, attributed to CoFe_2O_4 and diamagnetic contributions of SiO_2 and Au—see Figure 6.

$$M_T = xM_{\text{CoFe}_2\text{O}_4} - (y\chi_{\text{SiO}_2} + z\chi_{\text{Au}})H \quad (4)$$

By fitting the experimental data with the above relation, the contributions of CoFe_2O_4 to the nanostructure magnetizations were obtained. These values are in good agreement with the content of CoFe_2O_4 in the nanocomposites, as expected in the case of a simple magnetic dilution model—see Figure 9 and Table 1. The covering of the CoFe_2O_4 core with SiO_2 and Au shells do not induce changes in their magnetic properties as compared with that of the single CoFe_2O_4 phase. Thus, by varying the CoFe_2O_4 content in nanostructures it is possible to ensure the desired magnetic properties of nanocomposites.

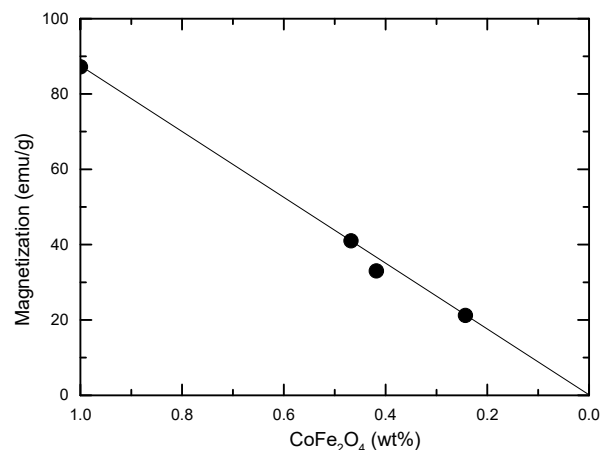


Figure 9. Magnetizations at $T = 4.2$ K as a function of CoFe_2O_4 content in $\text{CoFe}_2\text{O}_4@SiO_2@AuN$ nanocomposites. The solid line gives the expected trend in a simple dilution magnetic model.

The diamagnetic contributions of the SiO_2 and Au content, as determined from VSM studies, are higher than those expected starting from those of bulk SiO_2 and Au, $\chi_{\text{SiO}_2} = 0.447 \times 10^{-6}$ [30] and $\chi_{\text{Au}} = 2.74 \times 10^{-6}$ [31], respectively. Unlike that of Au, the diamagnetism of SiO_2 is not affected by the nanocrystalline sizes. A giant diamagnetism has been observed already in gold nanorods [32] and theoretically investigated [33,34]. After the subtraction of the contribution of SiO_2 to nanostructural diamagnetism, the diamagnetic

susceptibility of gold nanoparticles was shown to be higher by one order of magnitude than that of the bulk value.

The giant diamagnetic susceptibility of gold nanoparticles is a consequence of field-induced currents in the surface electrons [33]. The diamagnetic susceptibility is originated by steady currents induced by the applied field for quasi-free electrons confined in the surface. The diamagnetic response, induced when the external field is turned on, remains constant during the time the field is acting. As the size of the sample increases, the percentage of surface atoms decreases. Consequently, the magnetism of the surface approached that of the bulk sample. Such a trend is evidenced by the present data. The diamagnetism of gold nanoparticles, in relative units $s = \chi_{\text{ex,Au}}/\chi_{\text{Au}}$, is plotted in Figure 10, as a function of nanocrystallites surfaces, assuming that these have a spherical form. On the same figure, the s parameter determined for a nanorod with $d = 15$ nm and $l = 80$ nm is also given [32]. These data are in agreement with the expected trend between gold diamagnetism and nanoparticle dimensions

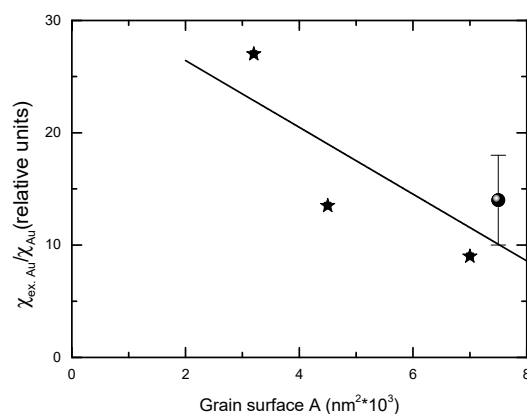


Figure 10. The gold diamagnetism in $\text{CoFe}_2\text{O}_4@\text{SiO}_2@\text{AuN}$ nanostructures as function of the mean surface of Au nanograins, in relative units (referred to bulk gold diamagnetism) (*). The data from [31] are also given (●).

The coercivities of CoFe_2O_4 and $\text{CoFe}_2\text{O}_4@\text{SiO}_2@\text{AuN}$ nanostructures determined from hysteresis loops, recorded at 4.2 K and 300 K, are given in Table 1. The coercive fields at $T = 4.2$ and 300 K increase due to reduction in CoFe_2O_4 nanosizes. At ambient temperatures, these values are smaller by one order of magnitude than those determined at $T = 4.2$ K. These magnetic measurements fail to fully describe complex magnetic nanostructures, such as an ensemble of nanoparticles with different magnetic properties, mainly due to the size distribution of the grains. The first-order reversal curve (FORC) diagram offers an image related to the coercivity and interaction fields acting on the different magnetic entities within the sample [35–38]. After applying a magnetic field to ensure the saturation magnetization, this is reduced to a predefined field H_r , denoted as the reversal field, and the magnetization of the sample is measured while H is returned. The above sequence is repeated with a decreasing H_r , thus obtaining a sequence of magnetization curves $M(H_r, H)$. On this basis, the FORC distribution, P , defined as a second derivative of the magnetization with respect to reversal and applied field, is obtained. The quantitative analysis of the FORC data is performed using the projection of the FORC distribution in the plane of the coercive field, $H_c = (1/2)(H - H_r)$, and the interaction field, $H_u = (1/2)(H + H_r)$, axes, called the coercivity distribution (P_{Hc}) and interaction distribution (P_{Hu}), respectively. The FORC distributions for the CoFe_2O_4 and $\text{CoFe}_2\text{O}_4@\text{SiO}_2@\text{Au}_2$ nanostructures are given in Figure 11. In CoFe_2O_4 nanograins, there is a large distribution of coercive fields and interaction fields.

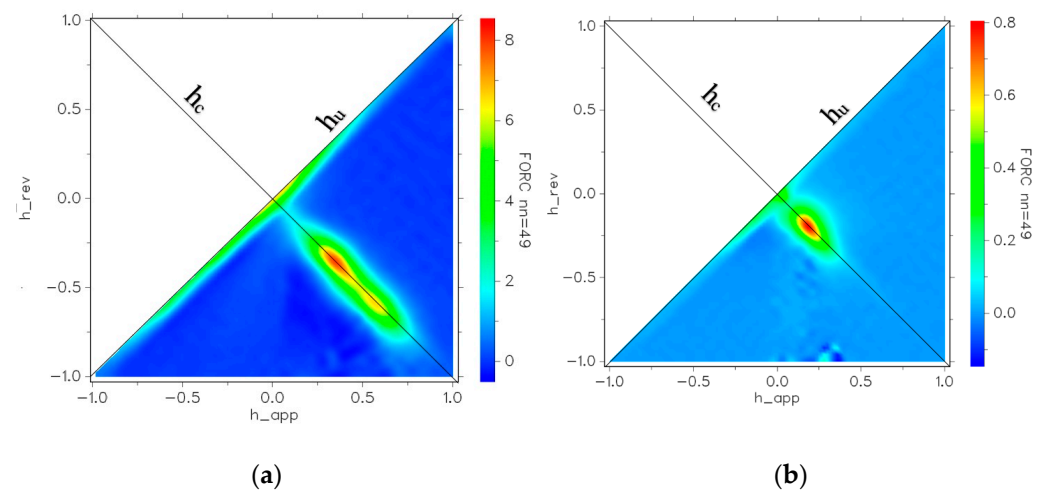


Figure 11. FORC diagrams for CoFe_2O_4 (a) and $\text{CoFe}_2\text{O}_4@SiO_2@Au_2$ (b) nanocomposites. h_{rev} denotes the applied field for each inversion curve. h_{app} is the applied field after that inversion is realized. nn is the smoothing factor.

The latter is due to particle interactions and the former is due to different particles switching at different applied field strengths. A higher maximum in the p value indicates stronger exchange interactions. The maximum of the probability density for CoFe_2O_4 is one order of magnitude larger than that for $\text{CoFe}_2\text{O}_4@SiO_2@AuN$. This means that the FORC distribution of CoFe_2O_4 is much narrower than that for $\text{CoFe}_2\text{O}_4@SiO_2@AuN$ nanocomposites. The extended spot shown in the FORC diagram of CoFe_2O_4 resembles “single phase” behavior, but with large exchange interactions between the nanograins along the h_c -axis. In $\text{CoFe}_2\text{O}_4@SiO_2@Au_2$ nanostructures, the peak distribution is located at an interaction field of 0.19 T. The peak in the FORC distribution is thus shifted towards positive reversal and interaction fields in the core–shell nanostructures, dipolar interactions being increasingly more important due to the presence of a SiO_2 -Au shell and its screening effect.

4. Conclusions

Magnetoplasmonic $\text{CoFe}_2\text{O}_4@SiO_2@Au$ nanoparticles were successfully prepared. The SiO_2 shell was mainly in an amorphous state, as evidenced in XRD patterns by a broad feature at low angles. The lattice constants of CoFe_2O_4 and Au were not dependent on nanostructure compositions being close to those of bulk samples. The crystallite sizes of CoFe_2O_4 nanoparticles were in the 14.2 nm and 20.2 nm range, while those of gold were between 15.9 nm and 23.6 nm. The TEM and SEM images of CoFe_2O_4 nanoparticles evidenced that these are of nearly spherical form and agglomerate in separate pseudo-spherical “raspberry”-like nanostructures. The presence of a spin-glass contribution superposed on mainly ferrimagnetic-type ordering is suggested. The contribution of the spin-glass state to magnetization was no more than 8% of the total CoFe_2O_4 nanoparticle magnetization. This could have been due to the cumulative effects of the broken exchange bonds at the surface layer, as well as to the exchange interactions between constituent ions. As a function of the external magnetic field, two types of spin-glasses were observed and correlated with different exchange fields acting on tetrahedral and octahedral iron sites.

The diamagnetic susceptibility of gold nanoparticles was shown to be by one order of magnitude higher than that of the bulk value. The giant diamagnetic susceptibility of gold nanoparticles is a consequence of field induced currents in the surface electrons. The diamagnetic susceptibility originated by the steady currents induced by the applied field for quasi-free electrons was confined in the surface. As the size of the sample increased, the percentage of surface atoms decreased. Consequently, the diamagnetism approached that of the bulk sample.

The FORC diagram of CoFe_2O_4 highlighted “single phase” behavior, with large exchange interactions between the nanograins along the h_c -axis. The peak in the FORC

distribution was shifted towards positive reversal and interaction fields in the core-shell nanostructures, dipolar interactions increasing due to the presence of SiO₂@Au shells and their screening effects.

Author Contributions: Conceptualization, R.T., R.S. and E.B.; investigation, R.B., A.S., G.S., R.D., R.H., L.B.-T. and V.T.; resources, R.B., A.S. and R.T.; formal analysis, R.B., G.S., R.D., R.H., E.B.; writing—original draft preparation, R.B., R.T., E.B.; writing—review and editing, E.B., R.S., R.T.; visualization, R.B., R.T.; supervision, R.T., E.B.; project administration, E.B., R.T., R.S.; funding acquisition, E.B., R.S. and R.T. All authors have read and agreed to the published version of the manuscript.

Funding: This research was funded by the Romanian National Authority for Scientific Research, CNCSIS-UEFISCDI, through the exploratory research project No. PN-III-P4-ID-PCCF-2016-0112.

Institutional Review Board Statement: Not applicable.

Informed Consent Statement: Not applicable.

Data Availability Statement: Not applicable.

Conflicts of Interest: The authors declare no conflict of interest.

References

1. Sawatzky, G.A.; Van Der Woude, F.; Morrish, A.H. Mössbauer Study of Several Ferrimagnetic Spinel. *Phys. Rev.* **1969**, *187*, 747–757. [[CrossRef](#)]
2. Srivastava, C.M.; Srinivasan, G.; Nanadikar, N.G. Exchange constants in spinel ferrites. *Phys. Rev. B* **1979**, *19*, 499–508. [[CrossRef](#)]
3. Chinnasamy, C.N.; Jeyadevan, B.; Shinoda, K.; Tohji, K.; Djayaprawira, D.J.; Takahashi, M.; Joseyphus, J.; Narayanasamy, A. Unusually high coercivity and critical single-domain size of nearly monodispersed CoFe₂O₄ nanoparticles. *Appl. Phys. Lett.* **2003**, *83*, 2862–2864. [[CrossRef](#)]
4. Sun, Q.-C.; Birkel, C.S.; Cao, J.; Tremel, W.; Musfeldt, J.L. Spectroscopic signature of the superparamagnetic transition and surface spin disorder in CoFe₂O₄ nanoparticles. *ACS Nano* **2012**, *6*, 4876–4883. [[CrossRef](#)] [[PubMed](#)]
5. Peddis, D.; Yaacoub, N.; Ferretti, M.; Martinelli, A.; Piccaluga, G.; Musinu, A.; Cannas, C.; Navarra, G.; Greneche, J.-M.; Fiorani, D. Cationic distribution and spin canting in CoFe₂O₄ nanoparticles. *J. Phys. Condens. Matter* **2011**, *23*, 426004. [[CrossRef](#)]
6. Peddis, D.; Cannas, C.; Musinu, A.; Piccaluga, G. Coexistence of superparamagnetism and spin-glass like magnetic ordering phenomena in a CoFe₂O₄–SiO₂ nanocomposite. *J. Phys. Chem. C* **2008**, *112*, 5141–5147. [[CrossRef](#)]
7. Chiu, C.-W.; Lin, P.-H. Core/shell Ag@silicate nanoplatelets and poly(Vinyl Alcohol) spherical nanohybrids fabricated by coaxial electrospinning as highly sensitive SERS substrates. *RSC Adv.* **2016**, *6*, 67204–67211. [[CrossRef](#)]
8. Prabhakaran, T.; Mangalaraja, R.; Denardin, J.; Jiménez, J.A. The effect of reaction temperature on the structural and magnetic properties of nano CoFe₂O₄. *Ceram. Int.* **2017**, *43*, 5599–5606. [[CrossRef](#)]
9. Kiran, B.L.; Rami, R.Y.V. Synthesis and characterization of magnetically core-shell structured CoFe₂O₄/SiO₂ nanoparticles; Their enhanced antibacterial and electrocatalytic properties. *Coll. Surf. A Physicochem. Eng. Asp.* **2020**, *598*, 124806. [[CrossRef](#)]
10. Lin, Y.-S.; Haynes, C.L. Synthesis and characterization of biocompatible and size-tunable multifunctional porous silica nanoparticles. *Chem. Mater.* **2009**, *21*, 3979–3986. [[CrossRef](#)]
11. Cannas, C.; Musinu, A.; Ardu, A.; Orrù, F.; Peddis, D.; Casu, M.; Sanna, R.; Angius, F.; Diaz, G.; Piccaluga, G. CoFe₂O₄ and CoFe₂O₄/SiO₂ core/shell nanoparticles: Magnetic and spectroscopic study. *Chem. Mater.* **2010**, *22*, 3353–3361. [[CrossRef](#)]
12. Parma, A.; Freris, I.; Riello, P.; Cristofori, D.; Fernández, C.D.J.; Amendola, V.; Meneghetti, M.; Benedetti, A. Structural and magnetic properties of mesoporous SiO₂ nanoparticles impregnated with iron oxide or cobalt-iron oxide nanocrystals. *J. Mater. Chem.* **2012**, *22*, 19276–19288. [[CrossRef](#)]
13. Carlà, F.; Campo, G.; Sangregorio, C.; Caneschi, A.; Fernández, C.D.J.; Cabrera, L.I. Electrochemical characterization of core@shell CoFe₂O₄/Au composite. *J. Nanoparticle Res.* **2013**, *15*, 1–16. [[CrossRef](#)]
14. Zhang, X.; Niu, Y.; Zhao, J.; Li, Y. Fabrication, structures and molecule detection of gold films coated on γ-Fe₂O₃@SiO₂ ellipsoid ordered arrays. *Coll. Surf. A Physicochem. Eng. Asp.* **2017**, *520*, 343–347. [[CrossRef](#)]
15. Kassim, S.; Tahrin, R.A.A.; Harun, N.A. Metallic Core-Shell Photonic Crystals for Surface-Enhanced Raman Scattering (SERS). *Plasmonics* **2020**, *15*, 1499–1505. [[CrossRef](#)]
16. Li, Y.; Duan, W.; Wei, J. CoFe₂O₄/Ag nanostructures as highly sensitive surface-enhanced raman scattering substrates. *ACS Appl. Nano Mater.* **2021**, *4*, 4181–4188. [[CrossRef](#)]
17. Huynh, K.-H.; Hahm, E.; Noh, M.; Lee, J.-H.; Pham, X.-H.; Lee, S.; Kim, J.; Rho, W.-Y.; Chang, H.; Kim, D.; et al. Recent advances in surface-enhanced raman scattering magnetic plasmonic particles for bioapplications. *Nanomaterials* **2021**, *11*, 1215. [[CrossRef](#)] [[PubMed](#)]
18. Dudric, R.; Souca, G.; Szatmári, Á.; Szilárd, T.; Nitica, S.; Iacovita, C.; Moldovan, A.I.; Stiufluic, R.; Tetean, R.; Burzo, E. Magnetite nanoparticles for medical applications. *AIP Conf. Proc.* **2020**, *2218*, 030014. [[CrossRef](#)]

19. Souca, G.; Dudric, R.; Iacovita, C.; Moldovan, A.; Frentiu, T.; Stiufiuc, R.; Lucaciu, C.M.; Tetean, R.; Burzo, E. Physical properties of Zn doped Fe₃O₄ nanoparticles. *J. Optoelectron. Adv. Mater.* **2020**, *22*, 298–302.
20. Tejada, J.; Martinez, B.; Labarta, A.; Chudnovsky, E.M. Correlated spin glass generated by structural disorder in the amorphous Dy₆Fe₇₄B₂₀ alloy. *Phys. Rev. B* **1991**, *44*, 7698. [[CrossRef](#)]
21. Serrate, D.; De Teresa, J.M.; Algarabel, P.A.; Ibarra, M.R.; Galibert, J. Intergrain magnetoresistance up to 50 T in the half-metallic (Ba_{0.8}Sr_{0.2})₂FeMoO₆ double perovskite: Spin-glass behavior of the grain boundary. *Phys. Rev. B* **2005**, *71*, 104409. [[CrossRef](#)]
22. Burzo, E.; Balasz, I.; Valeanu, M.; Pop, I. The effects of thermal treatment on the physical properties of Sr₂FeMo_{1-x}MxO₆ perovskite with M=W, Ta and 0.3. *J. Alloy. Compd.* **2011**, *509*, 105–113. [[CrossRef](#)]
23. Burzo, E. Magnetic and transport properties of double perovskites. *Stud. Univ. Babeş-Bolyai. Chem.* **2021**, *66*, 63–72. [[CrossRef](#)]
24. Concas, G.; Spano, G.; Cannas, C.; Musinu, A.; Peddis, D.; Piccaluga, G. Inversion degree and saturation magnetization of different nanocrystalline cobalt ferrites. *J. Magn. Magn. Mater.* **2009**, *321*, 1893–1897. [[CrossRef](#)]
25. Venturini, J.; Tonelli, A.M.; Wermuth, T.B.; Zampiva, R.Y.S.; Arcaro, S.; Viegas, A.D.C.; Bergmann, C.P. Excess of cations in the sol-gel synthesis of cobalt ferrite (CoFe₂O₄): A pathway to switching the inversion degree of spinels. *J. Magn. Magn. Mater.* **2019**, *482*, 1–8. [[CrossRef](#)]
26. Caruntu, D.; Caruntu, G.; O'Connor, C.J. Magnetic properties of variable-sized Fe₃O₄ nanoparticles synthesized from non-aqueous homogeneous solutions of polyols. *J. Phys. D Appl. Phys.* **2007**, *40*, 5801–5809. [[CrossRef](#)]
27. Stoner, E.C.; Wohlfarth, E.P. A mechanism of magnetic hysteresis in heterogeneous alloys. *Philos. Trans. R. Soc. Lond. Ser. A Math. Phys. Sci.* **1948**, *240*, 599–642. [[CrossRef](#)]
28. Gittleman, J.I.; Abeles, B.; Bozowski, S. Superparamagnetism and relaxation effects in granular Ni-SiO₂ and Ni-Al₂O₃ films. *Phys. Rev. B* **1974**, *9*, 3891. [[CrossRef](#)]
29. Omelyanchik, A.; Salvador, M.; D'Orazio, F.; Mameli, V.; Cannas, C.; Fiorani, D.; Musinu, A.; Rivas, M.; Rodionova, V.; Varvaro, G.; et al. Magnetocrystalline and surface anisotropy in CoFe₂O₄ nanoparticles. *Nanomaterials* **2020**, *10*, 1288. [[CrossRef](#)] [[PubMed](#)]
30. Kondrashova, N.; Valtsifer, V.; Strelnikov, V.; Mitrofanov, V.; Uporov, S. Magnetic Properties of Silica with Mesopores as MCM-48. 2015. Available online: <https://www.ariel.ac.il/sites/conf/mmt/ws2015/service%20files/papers/124-130.pdf> (accessed on 19 February 2022).
31. Henry, W.G.; Rogers, J.L. XXI. The magnetic susceptibilities of copper, silver and gold and errors in the Gouy method. *Philos. Mag.* **1956**, *1*, 223–236. [[CrossRef](#)]
32. Van Rhee, P.G.; Zijlstra, P.; Verhagen, T.G.A.; Aarts, J.; Katsnelson, M.I.; Maan, J.C.; Orrit, M.; Christianen, P.C.M. Giant magnetic susceptibility of gold nanorods detected by magnetic alignment. *Phys. Rev. Lett.* **2013**, *111*, 127202. [[CrossRef](#)]
33. Hernando, A.; Ayuela, A.; Crespo, P.; Echenique, P.M. Giant diamagnetism of gold nanorods. *New J. Phys.* **2014**, *16*, 073043. [[CrossRef](#)]
34. Roda-Llodes, M.; Gonzalez-Ballester, C.; López, A.E.R.; Martínez-Pérez, M.J.; Luis, F.; Romero-Isart, O. Quantum size effects in the magnetic susceptibility of a metallic nanoparticle. *Phys. Rev. B* **2021**, *104*, L100407. [[CrossRef](#)]
35. Kouhpanji, M.R.Z.; Stadler, B.J.H. Beyond the qualitative description of complex magnetic nanoparticle arrays using FORC measurement. *Nano Express* **2020**, *1*, 010017. [[CrossRef](#)]
36. Muxworthy, A.; Heslop, D.; Williams, W. Influence of magnetostatic interactions on first-order-reversal-curve (FORC) diagrams: A micromagnetic approach. *Geophys. J. Int.* **2004**, *158*, 888–897. [[CrossRef](#)]
37. Tanasa, R.; Stancu, A. Statistical Characterization of the FORC Diagram. *IEEE Trans. Magn.* **2006**, *42*, 3246–3248. [[CrossRef](#)]
38. Dodrill, B.; Ohodnicki, P.; McHenry, M.; Leary, A. High-Temperature First-Order-Reversal-Curve (FORC) Study of Magnetic Nanoparticle Based Nanocomposite Materials. *MRS Adv.* **2017**, *2*, 2669–2674. [[CrossRef](#)]